

<sup>1</sup> Masters Thesis: The Evolution of Fault Slip  
<sup>2</sup> Surfaces with Cumulative Displacement

<sup>3</sup> Kelian Dascher-Cousineau

<sup>4</sup> April 28, 2017

<sup>5</sup> **Abstract**

<sup>6</sup> Fault slip surface roughness determines fault strength, friction and dy-  
<sup>7</sup> namic fault processes. Wear models and field observations suggest that  
<sup>8</sup> roughness decreases with cumulative displacement. However, measurements  
<sup>9</sup> have yet to isolate the effect of displacement from other possible controls,  
<sup>10</sup> such as lithology or tectonic setting. We present an unprecedentedly large  
<sup>11</sup> fault surface dataset collected in and around the San-Rafael Desert, S.E.  
<sup>12</sup> Utah, United States. In the study area, faults accommodated regional ex-  
<sup>13</sup> tension at shallow 1 to 3 *km* depth and are hosted in the massive, well  
<sup>14</sup> sorted, high porosity Navajo and Entrada sandstones. Existing detailed  
<sup>15</sup> stratigraphic throw profile provide a maximum constraint for displacement.  
<sup>16</sup> Where cross-sectional exposure is good, we measure exact displacement im-  
<sup>17</sup> parted on slip surfaces using offset in marker horizons. Thereby, we isolate  
<sup>18</sup> for the effect of displacement during the embryonic stages of faulting (0 to  
<sup>19</sup> 60 *m* in displacement). Our field observations indicate a clear compositional

and morphological progression from isolated joints or deformation bands towards smooth, continuous and mirror-like fault slip surfaces with increasing displacement. To quantify these observations, slip surfaces were scanned with a white light interferometer, a laser scanner and a ground based Li-dar. Together these instruments resolve more than eight decades of spatial bandwidth (from less than  $\mu\text{m}$ 's to  $\text{m}$ 's in scale). Results indicate that roughness as defined by the power ( $P$ ) at a given wavelength ( $\lambda$ ) decreases with displacement ( $D$ ) according to a power law,  $P(\lambda) \propto D^{0.6 \pm 0.1}$ . Trends are however subject to significant scatter. Roughness measurement associated with only maximum constraints on displacements corroborate this result—for a given displacement, minimum roughness is bounded by the later smoothing trend. In addition, we find that the maximum roughness is fixed—bounded a by a primordial roughness corresponding to that of joints surfaces and deformation band edges. Building upon our results, we propose a wear model to explain the evolution of faults with displacement. The basis of the model is supported by numerical simulations of crack initiation and growth using boundary element models Fri2D and growth by work-minimization (GROW). Our modelling provides the first insight into fault slip surface process consistent with observational constraints, i.e. fractal geometry and a nearly power-law decay with displacement, by using calling upon scale dependent strength, strength heterogeneity and scale invariant asperity failure by truncation.

<sup>42</sup> **Contribution of Authors**

<sup>43</sup> **1 Introduction**

<sup>44</sup> Faults are a characteristic feature of the Earth's brittle crust. Fluid flow, seismicity  
<sup>45</sup> and crustal mineralization are just few systems upon which faults act as major  
<sup>46</sup> controls [?] (more citations...). In spite of their importance, some aspects of faults  
<sup>47</sup> and their underlying processes remain poorly understood. How strong is a fault?  
<sup>48</sup> How do faults mature? Are small faults mechanically different to large faults?  
<sup>49</sup> Fault geometry has been shown to be a key parameter controlling the mechanical  
<sup>50</sup> behavior and evolution of faults (e.g. [?] [?] [?] [?]), but these questions are not  
<sup>51</sup> yet fully answered.

<sup>52</sup> Slip on a fault occurs on discrete slip surfaces in fault zones [?]. These surfaces  
<sup>53</sup> are not planar; they are rough. Roughness is observable at all scales [?] [?].  
<sup>54</sup> Slickenlines, corrugations, mullions and jogs are all surface features that can be  
<sup>55</sup> seen at different length scales [?]. Field studies have found common characteristics  
<sup>56</sup> in the topography of fault surfaces. These can be summarized as follows: 1) Fault  
<sup>57</sup> surfaces appear to be well defined by large fractal domains, wherein 2) faults  
<sup>58</sup> are smoother at larger length scales [?] [?], 3) rougher in the slip perpendicular  
<sup>59</sup> direction than in the slip parallel direction [?] and 4) slip surfaces are smoother  
<sup>60</sup> with cumulative displacement [?] [?]. Fault roughness has been demonstrated to  
<sup>61</sup> be critical in determining the strength [?] [?], triggering [?], dynamic properties [?];  
<sup>62</sup> Dunham et al., 2011), spatial distribution (Parson, 2008) and failure recurrence of  
<sup>63</sup> faults (Stirling et al., 1996). It is increasingly evident that roughness is a fingerprint  
<sup>64</sup> of fundamental features of the faulting process [?] [?]. In accordance, incorporating

more complex sources geometries has become a more frequent practice in dynamic earthquake rupture modelling [?].

Changes in roughness, as determined by cumulative displacement (Sagy et al., 2007; Brodsky et al., 2011), imply faults mature. Fundamental differences between immature and mature fault have far-reaching implications. Fixed source parameter scaling of earthquakes is a pillar of earthquake seismology. However, analysis of seismic signals of immature faults vs. mature faults suggest that scaling is sensitive to cumulative displacement. This observation leads to an interpretation of fundamental differences in earthquake populations. Specifically fault maturation would undermine the applicability of a constant magnitude scaling. Evolving mechanical properties such as fault friction and static strength—both associated to fault roughness—would imply that immature and mature faults belong to distinct populations with distinct scaling. (Harrington and Brodsky, 2011)

While there has been significant progress in understanding the role of roughness in the faulting process, how and why fault surfaces change is still unclear (e.g. [?], [?]). Sagy et al. (2007) noted a systematic decrease in roughness of ‘mature’, large displacement faults compared to ‘immature’ faults with low displacements. Similar results have since been observed along reactivated joints, in laboratory experiments (Davidesko et al., 2014), and in compilations of fault roughness analysis (Brodsky et al., 2011; Candela et al., 2012). These studies all attribute the decrease in roughness to wear at the fault interface. However, these data show only weak correlations between fault roughness and cumulative displacement. Indeed, relating roughness and cumulative displacement is not trivial. Fault surfaces in exhumed faults are rarely well preserved. Furthermore, obtaining well-constrained displacement estimates is contingent on the presence of precise

90 and accurate displacement kinematic indicators. Combining observations over a  
91 broad range of displacements is challenging. Consequently, it is unclear whether  
92 trends observed in compilations of roughness measurements from multiple faults  
93 are directly attributable to displacement or a combination other geological factors.  
94 For instance, while comparing fault surfaces from geologically diverse datasets,  
95 variations in lithology, faulting mechanism, temperature and depth may all be  
96 introducing further systematic variations.

97 \*this paragraph may not make sense anymore\*

98 Additionally, the evolution of roughness represents a novel insight into the  
99 architecture of a fault zone. The geometry of the fault surface modulates the  
100 architecture of the whole fault zone (Mitchell and Faulkner, 2009). Changes in  
101 roughness require interaction between the slip surfaces and its direct surrounding  
102 (fault core), resulting in the formation of fault rock (Power and Tullis, 1988). In  
103 addition to earthquake mechanics, the architecture of a fault zone, and its cor-  
104 responding permeability structure, is very important for hydrocarbon exploration  
105 (Shipton and Cowie, 2003). The production of wear material is inherently tied to  
106 changes in the slip surface geometry through wear processes, the fault rock, is also  
107 poorly understood. Fault rock thickness growth with displacement is documented  
108 (Sholtz, 1987; how thick is a fault... et al), but variability is such that even order  
109 of magnitude estimates of thickness for a given displacement are unavailable.

110 In this study, we report on how fault surfaces change. Scan measurements are  
111 taken in Southern Utah on pristine fault surfaces with terrestrial laser scanners and  
112 hand-samples for laboratory high resolution scans. We quantify the roughness from  
113 the scan measurements. These estimates correlated with displacements confirm  
114 and better quantify the role of cumulative displacement on fault roughness. Our

115 robust quantitative correlation between roughness and cumulative displacement  
116 educates and offers means to educate and parametrize a semi-analytical wear model  
117 for fault surfaces.

118 In the following report, we first outline methods to quantify fault roughness.  
119 We then motivate

## 120 1.1 Fault Roughness

121 The deviation from planarity formally defines roughness (Brown and Scholz, 1985).  
122 Pioneering studies used contact profilometers to measure the roughness of fault  
123 surfaces (Scholz and Aviles, 1986; Power and Tullis, 1991. Combined with sur-  
124 face profiles of large scale continental faults, faults were found to have a remark-  
125 ably broad fractal band ranging over 10 orders of magnitude—from  $10^{-5}$  to  $10^5 m$   
126 (Scholz and Aviles, 1986). Over these length scales, fractal scaling is said to be  
127 statistically self-affine. A statistically self-affine profile along  $x$  with heights  $h(x)$ ,  
128 is invariant under the affine transformation:

$$\begin{cases} x \rightarrow \lambda x \\ h \rightarrow \mu h \end{cases} \quad (1)$$

129 This relation therefore implies an exponential relation between the scaling,  $\lambda$   
130 (along  $x$ ), and  $\mu$  (along  $h$ ) such that:

$$\mu = \lambda^\varsigma \quad (2)$$

131 Where  $\varsigma$  is a constant named the Hurst exponent. Note that self-similarity,  
132 is an instance of self-affinity where the Hurst exponent is 1 (Schmittbulh et al.,

1993). Developments in laser scanner technology over the past decade, particularly terrestrial laser scanners, allowed surfaces to be characterized by calculating the Hurst exponent from thousands of cross sectional profiles through a fault surface (e.g. Candela et al., 2012). Studies of natural mode I crack surfaces have observed self-affinity with a Hurst exponent of  $\sim 0.8$  at all scales of observation (Scholtz, 1985). Shear, or mode II cracks (i.e. faults) are different. They are anisotropic—the Hurst exponent parallel to shear ( $\sim 0.6$ ) is smaller than that in the shear-perpendicular direction ( $\sim 0.8$ ) (Lee and Bruhn, 1996).

Another parameter is required to fully describe surface roughness. While the Hurst exponent describes the scaling behavior of the roughness it does not define the magnitude of the roughness. The pre-factor defines the amplitude of the scaling law (Candela et al., 2009). The pre-factor is subject to significant variation. Overall, observations show that fault surfaces have distinctly smoother profiles along slip direction than perpendicular to slip (Lee and Bruhn, 1996). Many methods exist to quantify roughness scaling, possibly most intuitive of which is the Root Mean Squared (*RMS*) as a function of scale. For a profile of length  $L$  with a point spacing of  $\Delta x$  with deviation  $h$  from the best fit line, the *RMS* for a given scale  $s$  is defined as follows:

$$RMS(s) = \sqrt{\frac{\Delta x}{L} \sum_{i=1}^{L/\Delta x} h_i^2} \quad (3)$$

The *RMS* roughness of a fault or fracture exhibits power-law scaling with segment length. A self-affine profile should therefore plot as a straight line on a log-log plot of the *RMS* as a function of the segment length with a slope equivalent to the Hurst exponent. (Schmittbuhl et al., 1993) The power spectrum of a surface

profile has been shown to yield more robust roughness metrics (Schmittbuhl et al., 1993; Candela et al., 2009). For a set of discretely sampled points, the power spectrum of a profiles is the result of a Fast Fourier Transform (FFT). The spectrum defines the surface profile as superposition of sinusoidal profiles. In the frequency domain, rougher profiles will have correspondingly higher amplitudes, or power. The power spectrum,  $P(k)$ , of a self-affine profile (again in log-log space) defines a line as follows:

$$P(k) = Ck^{(-1-2\zeta)} \quad (4)$$

Where  $k$  is the frequency and  $C$  is the pre-factor (Candela et al., 2009).

## 1.2 The evolution of slip surfaces with displacement

\*this could be in an interpretation section

Previous work has mainly associated fault surface deformation to wear processes as the dominant mechanism of surface evolution [?] [?] [?]. It is worth recognizing that many other processes could also cause the slip surface to change. Surface evolution is not uniquely determined.

A surface can change according to the following:

*surface deformation*

*Addition of material*

*Removal of material*

Fault slip surfaces have evidence pointing to each of these processes preserved in the rock record.

175        *Surface deformation* is mainly enabled by plastic deformation processes. At  
176 seismogenic timescales, brittle deformation can occur—whereby macroscopic fault  
177 damage and microfractures in grains and crystals away from the fault can enable  
178 stain and dissipate stress on the fault. Equivalently at longer time-scales, calcite  
179 twinning, pressure solution, and clay alteration can also occur yield similar effects.  
180 These short and long-time scale mechanisms define the rheology of fault blocks.

181        It is unlikely that the rheology of the fault block and its effect on the slip  
182 surface topography are significant in the evolution of the slip surface. Using slick-  
183 enline orientations and fault core thickness as a proxy to the fault block rheology  
184 Kirkpatrick et al. 20??, find that 1) deformation does occurs in fault block and 2)  
185 there is a scale dependence to this deformation whereby. However, this scaling is  
186 not well represented in fault geometric scaling. It would rather predict a change  
187 in scaling at the outcrop scale. The absence of any such signal in the topography  
188 of fault slip surfaces (cite candela?) implies that deformational processes cannot  
189 directly determine how slip surfaces evolve with displacement.

190        For its part, an *addition of material* occurs as fault rock is cemented onto slip  
191 surfaces—filling in geometrical concavities and effectively reducing the amplitude  
192 of surface irregularities. Its effect is preserved in the rock record with mobile, or  
193 *fluidized*, gouge cemented and re-fractured in subsequent faulting (cite someone).  
194 It is key to note that this mechanism is metered by the healing rate and, the final  
195 surface deformations mechanism, the removal of material and the corresponding  
196 production of fault rock. The overall role of the addition of material on the final  
197 surface geometry is likely passive and minimal compared to its counterpart.

198        *removal of material* is caused by mechanical wear. As fault blocks slide past  
199 each other, frictional wear is an inevitable process. Layers of comminuted fault

200 rock, cemented or not, are direct evidence of this process [?] [?]. Wear is known to  
201 be multiscale. At small scales, grains can be plucked or broken (cite someone); at  
202 larger scales grains plough slip surfaces to create corrugations (cite someone), side-  
203 wall ripouts form [?] and branch lines can link anastamosing slip surfaces. It is key  
204 to note that all these processes fall under the definition of wear in that they involve  
205 the failure of geometrical asperities at various scales. Moreover, they have substantial  
206 impact on the surface geometry. MAKE FIGURE HERE FOR REFERENCE  
207 SIMILAR TO THE ONE IN YOUR EPSL SLICKENLINE/RHEOLOGY PAPER  
208 - but focus on the fact that there is an asperity failing.

209 While wear processes are subject of a vast field of research, particularly in en-  
210 gineering and tribology due to interest in lubricating and manufacturing machine  
211 parts for longevity (Meng and Ludema, 1995), its applications in the earth sci-  
212 ences is emergent with tests mainly conducted at laboratory scales (cite: Marone,  
213 faulkner, tullis, sholz). The only application to natural fault surfaces is a very  
214 rudimentary prediction of wear volume presented in [?].

215 Wear is formally defined as frictionally induced volume removal from surfaces  
216 in sliding contact. The wear rate, the amount of wear per unit distance is broadly  
217 related to the real area of contact and loading. When two surfaces are put in  
218 direct contact, the real area of contact is much smaller than the nominal surface  
219 areas because the load is supported at microscopic protrusions from a surface,  
220 called asperities. Remote loading normal to the surface causes local stresses and  
221 associated deformations at contact points. Note that as the load is increased,  
222 deformation of large asperities causes new asperities to come in contact. In its  
223 simplest form, wear rate defined as:

$$W \propto \frac{P}{a} \quad (5)$$

Where  $W$  is the wear rate,  $P$  is the remote load and  $a$  is a mean measure of the dimensions of the asperities in contact during sliding. The relation has been shown to be reasonably robust in experimentation for most materials. In further detail, the size, distribution and duration of contact areas, as well as the shape of the worn particles, control the general behaviour of wear. Note that material properties are contained in a constant of proportionality referred to as the probability factor—the probability of a collision of asperities to lead to removal of material (Holm, 1946; Archard, 1953).

If and how wear affect the geometry of a fault slip surface remains unclear. Both field and laboratory experiment show that wear is scale dependent, such that asperities are worn down at different rates according to their typical dimensions. Asperities at longer characteristic wavelengths and larger amplitudes wear down faster, on average, than those with small wave lengths and small amplitudes. These observations correspond to both a downward translation and potential clockwise rotation of the self-affine scaling in the power spectrum. The exact mechanism causing this behavior is unclear. Davidesko et al., 2014 suggest that dilation during displacement on a fault ‘shelters’ smaller, shorter wavelength, asperities and therefore wears down large, long wavelength asperities.

It is clear that the fractal nature of fault surfaces is important to reconcile with a model of wear. Fractal surfaces are difficult to integrate into the pre-existing framework of wear processes. Specifically, defining the real area of contact, corresponding deformation and, by association, the scale dependence of wear is non-

246 trivial (e.g. Persson, 2001; Jackson and Streator, 2006). Moreover, if wear is to  
247 represent the dominant mechanism that defines slip surface geometry, a common  
248 thread must exist between the processes outlined in figure XXX. Moreover, con-  
249 cepts of strength heterogeneity and scale dependent strength are poorly captured  
250 by the engineering literature. Caveats to simple wear models (i.e. Archard, 1953)  
251 exist. These include sensitivity to fault rock, sliding velocity and the presence of  
252 lubricant (e.g. pseudotachylite, amorphous silica gel and gouge). Moreover, the  
253 stresses imparted by a propagating fault rupture front are mechanically distinct  
254 from those related to rubbing surfaces. Such a distinction may also drastically alter  
255 the relation between wear material and the slip surface [?]. Since Archard (1953),  
256 models of wear tend to diverge in their results, assumptions and by association,  
257 their applicability (Meng and Ludema, 1995).

258 Efforts to model wear processes to understand faulting processes are very lim-  
259 ited. An analytical model forwarded by Wang and Scholtz 1994 ...

## 260 2 Geology

261 The San Rafael Desert hosts a sequence of gently dipping marine and sub-areal  
262 sedimentary rocks deposited from the Pennsylvanian to the Jurassic (see Figure 2).  
263 The San Rafael Desert is part of the San Rafael Swell, a monocline that formed  
264 when these sediments were uplifted as a passive drape fold above a reactivated  
265 basement reverse fault during the Late Cretaceous Laramide Orogeny (Kelly, 1955;  
266 Vrolijk et al., 2005). In turn, the swell is part of the broader Colorado Plateau  
267 (Kelly, 1955). Networks of joints and normal faults associated to further Laramide  
268 activity cross-cut sedimentary sequence accommodating North-South extension

(Aydin and Johnson, 1978; Vrolijk et al., 2005). Within the San Rafael Swell we focus the following field locations: 1) the Chimney Rock Fault Array, 2) the Big Hole fault and 3) a network of deformation bands in the Entrada formation near Goblin Valley State Park. Advantages of these field locations are manifold. First, the nearly pure quartzite lithology, extensional tectonic regime, depth (2-4 km or 40-80 MPa), temperature (estimates range from 45-90 °C) of activity, and faulting mechanism are all relatively consistent (Vrolijk et al., 2005). Consistency in these parameters is key to isolating the effect of displacement on the fault roughness. Moreover, both field locations exhibit well preserved fault surfaces that are exposed and accessible (see Figure 3).

The Chimney Rock fault array is an orthorhombic set of faults that crops out at the northern end of the San Rafael Swell ([?], Davatzes et al., 2003). Two pairs of oppositely dipping normal faults crop out at the surface with preserved fault scarps. WNW-striking faults are interpreted to have formed by shear reactivation of joints, whereas ENE-striking faults initially formed from deformation bands (Davatzes, 2003). Exposure is very good, faults are abundant and have well preserved fault surfaces (Vrolijk et al., 2005). The Chimney fault array has studied to better understand of fault geometry (Shipton and Cowie, 2001; Shipton and Cowie, 2003), permeability (Shipton et al., 2002) and kinematics ([?]; [?]; [?]; Davatzes et al., 2003) . As a result, detailed maps of the fault array have been produced (e.g. [?]) . In addition, by using measurements of the separation between footwall and hanging wall cutoffs of sedimentary horizons, entire displacement profiles have been measured for faults with a wide range of displacements (Cowie and Shipton, 1998; [?]; Shipton and Cowie 2001; Shipton and Cowie, 2003). The Big Hole fault is located just to the South-East of the Chimney Rock Fault Array.

While not explicitly part of the fault array, the Big Hole fault shares a nearly identical geological setting. The Big Hole fault has been extensively studied in detail as an analog to hydrocarbon reservoir-scale faults. Displacements on the exposed fault range from 8 m to 39 m. (Shipton and Cowie, 2001; Shipton and Cowie, 2003) Large networks of deformation band faults outcrop near Goblin Valley State Park on the southeastern margin of the San-Rafael Swell (Aydin and Johnson, 1978). Deformation bands are the result of concentrated shear deformation on narrow centimeter thick bands (Aydin and Johnson, 1978; Davatzes et al., 2003). Collapsing pore space, and grain crushing accommodates this deformation. Deformation bands are interpreted as the embryonic stages of fault development (Fossen and Hesthammer, 1998; Fossen et al., 2007). Because deformation bands dramatically alter the local permeability structure, Goblin Valley has been extensively studied in light of fault nucleation and the implications for hydrocarbon circulation (e.g. Fossen et al., 2005; Tobari and Fossen 2009). At Goblin valley, arrays of deformation bands anastomose—outcropping as centimeter- to meter-sized slabs. These are often bounded by discrete slip surfaces with well-preserved striations — i.e. roughness (Aydin and Johnson, 1978). Offsets in sedimentary beds have allowed previous studies to obtain detailed displacement measurements (e.g. Schultz and Fossen 2002). Together, these field locations offer the chance to survey well-preserved fault surfaces that have hosted displacements from embryonic stages to 30 m of displacement. Moreover, novel to this study, we are able to survey multiple expressions of a single fault's surface with various displacements according the displacement profile of the fault.



Loca- tion	Lithology	Description	Displacement Constraints
Chim- ney Rock Fault Array	At the contact between the Navajo Sandstone and the base of the Carmel Unit	Orthorombic set of normal faults with preserved faults scarps of Navajo Sandstone	Displacement profiled of stratigraphic throw constrained by offset on a Carmel Limestone Marker Horizon by Maerten et al., 2000.
91 317	Big Hole Fault	One single large normal fault structure partitioning displacement on two major strands traceable for kilometers through a river wash with scarp exposure, and strike parallel/perpendicular cross-sectional exposure	Displacement constrained using the top Erosionally competent horizon at the top of the Navajo by Shipton and Cowie, 2003 and directly where possible.
Iron Wash	Navajo Sandstone	Network of normal and strike-slip cross-cutting faults. Little scarp exposure but has good cross-sectional exposure with fresh slip surfaces (using hammer and chisle)	Displacement mostly constrained by direct measurement of offset in the Upper Navajo horizon.
Molly's Castle	Entrada Sandstone	East-West striking network of normal faults and ubiquitous deformation bands. Well preserved slip surfaces broadly	Displacement constraints available in places from mapping by Aydin (1978) and directly measured using various marker

Table 1: Table caption

### **319    3 Field observations and Microstructure**

320    We report on the fault architecture in the Navajo and Entrada Sandstones with  
321    a specific focus on the evolution from zero-displacement structures such as joints  
322    and deformation bands to large offset structures with polished slip surfaces and  
323    accompanying fault rock lithologies.

#### **324    3.0.1 Zero-Displacement Structures**

325    Deformations bands and joints are a ubiquitous and characteristic feature around  
326    faults in high porosity sandstones [?] [?]. Larger fault structures nucleated from  
327    pre-existing networks of deformation bands and joints [?]. Deformation local-  
328    izes and intensifies in and along these structures and eventually form through-  
329    going faults [?]. The characteristics and surface morphology of the local zero-  
330    displacement features are especially relevant to our analysis as they represent the  
331    original, zero displacement, roughness of faults in the study area. This is  
332    fundamental to understanding the integrated maturation path of slip surfaces to  
333    larger displacements

334    In outcrop, deformation bands, also known as shear bands are sinuous white  
335    lineaments, 1 to 5 millimeters in thickness, that accommodate small strain typi-  
336    cally as shear offset. Shear bands are a unique feature to coarse, well sorted  
337    sandstones. In sandstones, small strains can be accommodated by the localiza-  
338    tion of run-away collapse of grains in sub planar sheets [?]. In thinsection, bands  
339    are associated with a gradational reduction in grains size towards their centers  
340    (see figure ??). Grain size reduction is the result of comminution by crushing.  
341    In associations, grains are increasingly angular and packed. This change causes

342 deformation bands to erode differenctly than the host sandstone units [?]. De-  
 343 formation bands are stronger and more competant to erosion and often protrude  
 344 out of outcrop as thin sheets (see figure ??). Unlike the slip surfaces in the area,  
 345 deformation bands do not reduce the cohesion of the rock and accordingly do not  
 346 have well defined parting surfaces.

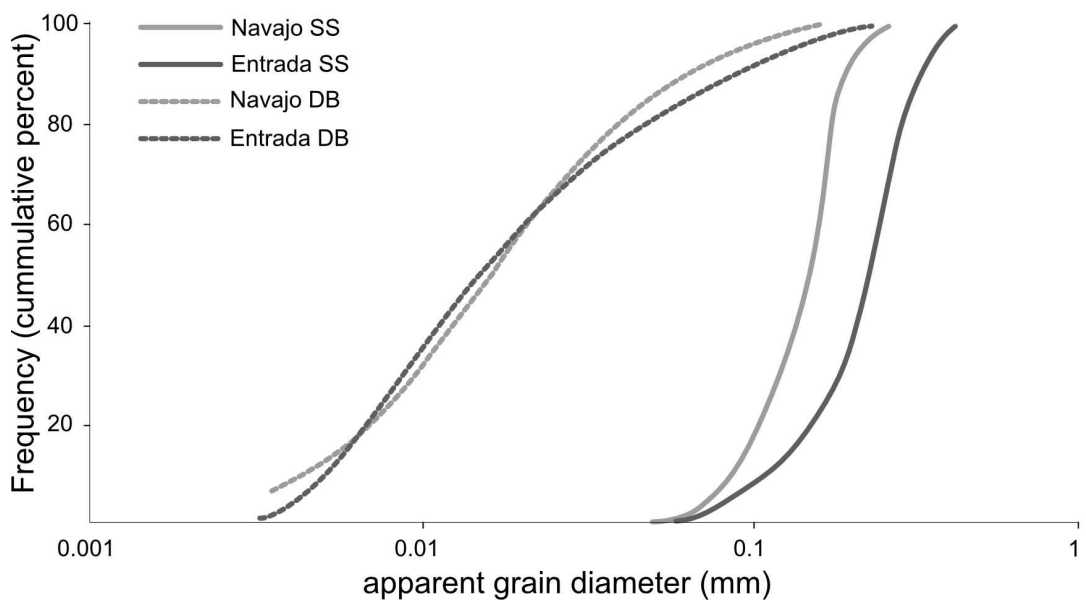


Figure 1: Grains size reduction of crushed grains within deformation bands relative to the undeformed sandstone units, the Navajo and Entrada sanstones. (figure adapted from Aydin, 1978)

347 Deformation bands often outcrop as coalesced nearly co-planar groups or clus-  
 348 ters. Deformation band cluster accommodate more intense and localized shear  
 349 strain. Larger clusters often have one or many through going slip surfaces. The  
 350 clusters are dense networks of anastamozing deformation bands ranging from a few



Figure 2: Example of single deformation bands protruding out of outcrop. A small deformation band cluster is also visible in the background.

351 millimetres to tens of centimetres in width, often outcropping as slabs up to meters  
 352 in sizes. This erosional feature is most clearly expressed in the Entrada Sandstone.  
 353 Clusters commonly form in upright conjugate pairs, each dipping around  $60^\circ$  in  
 354 opposite directions.

355 Edges of deformation band clusters that have eroded out appear to have dis-  
 356 tinctly corrugated and "lumpy" morphology (see figure ??-left). The orientation  
 357 of the corrugations is in clear agreement with the kinematics of through-going  
 358 slickensided slip surfaces. The slabs are coated with sand grains from the host  
 359 sandstone. There is a clear directional asymmetry along the direction of shear

360 whereby steep faces are in the direction of shear offset and shallowed faces are in  
361 the opposite directions (see figure ??). The asymmetry is observed on either side  
362 of deformation bands clusters. Refer to Fossen et al., 2007 and Aydin, 1978, for  
363 more detailed and very extensive characterizations of defomation bands in these  
364 localities.

365 Pre-existing regional joints sets are a common feature of every locality. Joints  
366 typically have dips near  $90^\circ$ . Joints set are best defined in the upper Navajo units  
367 and low Carmel limestone pavements. The intensity of joint increases near the  
368 fault with the occurrence of syn-kinematic sheared and splay joints [?]. Refer  
369 to Aydin and Davatzes, 2003, for extensive analysis of joint characteristics and  
370 relative timing for each locality.

371 The Entrada unit has more deformation bands and fewer and less well defined  
372 joints. Moreover, in the Chimney Rock fault array, there is a clear association to  
373 the conjugate fault set orientation. Faults striking



374 Figure 3: Left: Example of the edge of a deformation bands cluster at Molly’s  
375 Castle. Note the ”lumpy” morphology and an clear vertical directional asymmetry.  
376 Right: Cross-sectional view of a deformation band cluster with tens of centimeters  
377 of shear offset. It is unclear weather there is a through going slip surface localizing  
378 displacement. It is , however, definitely not on the edge of the cluster.

<sup>374</sup> **3.0.2 Slip Surfaces**

<sup>375</sup> Slip surfaces in the Navajo and Entrada sandstones are most readily identifiable  
<sup>376</sup> by their vitreous polish. Striations and grooves on the slip surfaces mark the  
<sup>377</sup> direction of slip. In Cross-section, slip surfaces are discrete, through-going and  
<sup>378</sup> smooth relative to their zero-displacement counterparts. Thin layers, less than  
<sup>379</sup> a few centimeters in thickness, of milky white layers bound typically bound the  
<sup>380</sup> slip surface. The slip surfaces often cross-cut or bound deformation band clusters.  
<sup>381</sup> For a given slip surface, perpendicular profiles are notably more sinuous than  
<sup>382</sup> slip parallel profiles. Slip surfaces are only preserved in the Navajo and Entrada  
<sup>383</sup> Sandstones. In spite of good exposures in prospecting pits and careful inspection  
<sup>384</sup> of the slip zone, the Navajo-Carmel contact at the Chimney Rock fault array did  
<sup>385</sup> not preserve good surfaces in the Carmel Unit. It is unclear whether this indicates  
<sup>386</sup> that the Carmel units is more susceptible to erosion and/or alteration; or if a  
<sup>387</sup> polished finish is only a feature of the quartzite sandstones. Pristine fault slip  
<sup>388</sup> surfaces are not cohesive, and readily form a parting surface. Fresh slip surfaces  
<sup>389</sup> uncovered *in situ* reveal a relatively consistent meso-structure (see figure – figure  
<sup>390</sup> similar to that in Jamies notes), A sharp interface, separated by a sub-mm thick  
<sup>391</sup> layer of incohesive white powder bounded by two vitreous surfaces is a dense set  
<sup>392</sup> of deformation bands.

<sup>393</sup> In spite of careful preparation using epoxy, thin sections all parted at the slip  
<sup>394</sup> surface interfaces. Moreover, samples only recording one side of the slip surfaces  
<sup>395</sup> only partially preserved the edge of the slip surface. Thin section observations reveal  
<sup>396</sup> a layered micro-structural architecture of the faults rock locally bound slip surfaces.  
<sup>397</sup> The following succession, ordered according to distance from the slip surface is

398 typical for slip surfaces in sand stone: 1) a very fine grained ultracataclastic layer,  
399 2) a broader comminuted layer (sometimes absent) and 3) a deformation band  
400 zone which grades into the intact protolith.

401 The ultacataclasite is continuous, nearly always bounds the slip surface, and  
402 ranges from sub-milimeter to 2 milimeters in thickness. Grain size distribution  
403 clearly has a steep fall off with most grains being unresolvable at 400 fold magni-  
404 fication. Larger grains are rounded to angular and do not exceed 10's of micron -  
405 significantly smaller than protolithic intact grains which are on the order of 100's  
406 of micron. Ultra-cataclasite layers show evidence of localized failure (see figure  
407 indicative of cycling between healing and brittle failure. Larger survivor grains  
408 within the layer are partially offset(see figure xxx). Ultra-cataclasite layers pre-  
409 serve a faint foliation oblique to the bounding intact rock. The kinamtics from  
410 the flow banding are consistent with sense of shear of grains protruding into the  
411 untra-cataclasite and partially sheared off. Previous work has shown no notable  
412 change in in the major elements, silicon, calcium, potassium and sodiu, of the  
413 undeformed sandstones [?].

414 The broader comminuted layer is not always present. Instead, the fault, still  
415 bounded by a thin ultra-cataclasite directly transitions into the intact host. When  
416 present, the comminuted layer is onset by a discontinuous interface with layer 1, the  
417 fine grained cataclasite. It is evidenced by a distinct change in grain size and spatial  
418 arrangement. Past this transition, grains are larger and preserve damaged but  
419 intact sedimentary textures from the sandstone. In contrast to the ultracataclasite,  
420 the original grain geometry is sometimes still discernible. Grains size within the  
421 comminuted layer is spatially variable with bands or lens' of larger grains separated  
422 by finer, more angular grains, texturally similar to deformation bands but showing

423 more advanced stages of grain size reductions and shear localizations.

424 The textural transition is best explained by dynamic grain size reduction and  
425 wear at the slip surface interface producing ultra-cataclasite which overprint more  
426 diffuse off-fault grain size reduction through grain crushing and deformation band  
427 production. This layer has highly variable thickness which typically ranges from  
428 millimetres to centimetres. Its thickness is asymmetric relative to the slip sur-  
429 face. Variability is directly associated to splay features which intensify mechanical  
430 damage around the fault. Dark oxide filled fractures up to a few centimetres in  
431 length abut steeply into the slip surface and over-print other fault-related textural  
432 features. These are characteristically consistent with dynamics tensile cracks and  
433 would correspondingly be indicative of seismic rupture velocities.

434 Scattered Electron Microscopy (SEM) reveals

435 Reddish-brown to dark tarnish and reduced vitreous lustres are indicative of  
436 advanced erosion. Sections of the slip surface are plucked off. Severely weathered  
437 scarps, not scanned in this study, develop a slip perpendicular fabric associated  
438 to conjugate fractures and deformation bands abutting into the slip surfaces. In  
439 the Chimney Rock Fault Array, lichen grew preferentially on north facing scarps.  
440 From our field observation, it is clear that erosion has the effect of re-roughening  
441 the slip surfaces, especially at smaller scales. We can confidently attribute these  
442 re-roughening effects to erosion because they did not occur in freshly parted slip  
443 surfaces.

444 The evolution of slip surfaces with displacement is qualitatively apparent.  
445 Faults with small displacements (centimetres of offset) are distinctly different than  
446 larger displacement faults (meters of offset). They are 1) visibly more sinuous, 2)  
447 laterally discontinuous, 3) less polished, instead, having a dull lustre, and 4) not

448 bounded by well-defined gouge or cataclasites layers bounding the slip surface vis-  
449 ible in the field. In spite of extensive investigation, we do not observe faults with  
450 well-defined slip surfaces with clear offset markers indicating less than approxi-  
451 mately half a centimetre of displacement. It is unclear whether this is the result of  
452 an undeveloped reductions in cohesion, as that associated to other slip surfaces ob-  
453 served in the field, or whether it is mechanically favorable to produce deformation  
454 bands at such low strain.

455 **3.0.3 Fault architecture**

456 Slickenline orientation of faults in the Navajo and Entrada sandstones indicate  
457 normal dip slip with some instances of strike slip offset. Rotation of the slip-  
458 direction typically neighbours point of fault intersection [?] [?]. Faults outcrop in  
459 relays and cross-cutting conjugate sets. We record dip angles ranging from  $44^\circ$  to  
460 sub-vertical with an average dip angle of  $70^\circ$ . The single slip surface accommodat-  
461 ing the bulk of stratigraphic offset is not systematically representative of the fault  
462 architecture. Often, fault zones instead have many slip surfaces, sheared joints and  
463 splays which partition offset. As is characteristic for high porosity sandstone [?],  
464 fault zones all have deformation bands. The intensity of deformation bands rapidly  
465 decreases with increasing distance from the fault. according to a power law away  
466 from the center of the fault zone and was shown to correlate in intensity with  
467 displacement on the fault . Deformation bands typically abut obliquely into the  
468 slip surfaces at shallow angles (less than  $70^\circ$ ).

469 Certain slip surfaces clearly accommodate the overwhelming majority of fault  
470 offset. Displacement accommodated by smaller neighbouring discontinuous slip  
471 surfaces is minimal (Shipton, XXX). Based on observations from previous workers

<sup>472</sup> and those made in this study where larger displacement slip surfaces are unam-  
<sup>473</sup> biguously identifiable allowed us to characteristically further its characteristics  
<sup>474</sup> generalized for the Navajo and Entrada Sanstones as follows:

- <sup>475</sup>     • *Large displacement faults are distinctly more discrete and planar.*
- <sup>476</sup>     • *Larger displacement faults are not cross-cut by deformation bands or more*  
<sup>477</sup>       *sinuous and discontinuous slip surfaces*
- <sup>478</sup>     • *in line with the implicit definition of a fault, the PSS is nearly cohesionless.*  
<sup>479</sup>       Locations identified to be expose section of a PSS inevitably cracked open  
<sup>480</sup>       when sampling across the slip surface—the slip surfaces had no cohesion.  
<sup>481</sup>       Cohesion is typically thought to reinstate by precipitation and healing. We  
<sup>482</sup>       did not observe recovered healing in this study.
- <sup>483</sup>     • *Large displacement faults have a vitreous finish;*
- <sup>484</sup>     • *Large displacement slip surfaces are typically in the center of a damage zone.*  
<sup>485</sup>       Damage in an inevitable consequence of displacement and the accompanying  
<sup>486</sup>       mismatch that accumulates. Damage at the field locations in this study is  
<sup>487</sup>       expressed as comminution (*e.g.* cataclasite and gouge), fragmentation (*e.g.*  
<sup>488</sup>       breccia, splay joints) and shear deformation (specifically deformation bands).

<sup>489</sup>       In this study, we refer to *fault rock* as rocks associated to a fault (Snoke et  
<sup>490</sup> al. 1998). We pay careful attention to the fault rock as it is inevitably coupled  
<sup>491</sup> to the slip surface roughness and its maturation with cumulative displacement.  
<sup>492</sup> The faults in our study area display a very diverse range in fault rock lithologies,  
<sup>493</sup> ranging from fine-grained cataclasites to massive bodies of breccias (up to meters  
<sup>494</sup> of thickness).

495        Fault rock consistently bounds slip surfaces—often asymmetrically. However,  
496        observations at the outcrop scale (10's of meters) both along the strike and dip  
497        indicate that both the lithology and thickness of the fault rock are highly heteroge-  
498        neous and are subject to large variability. These observations are consistent with  
499        more detailed fault architecture mapping conducted by Shipton et al., 2002.

500        We do not observe a clear and tractable relation between fault slip surface  
501        displacement and faults rock thickness. This is big part a result of difficulties in  
502        defining a clear fault rock thickness criterion which well encapsulates the variety  
503        of faults rocks – a challenge well highlighted in (Shipton et al., 2006).

504        \* this stuff is left over's from editing and moving things around

505        Healed Gouges - the spot at big hole - iron wash (powder between the surface)  
506        - micro-structure - prospecting pit - typically on thinned sections of the fault rock  
507        (near the slip surface) Cataclasites .... - big hole sample with slip surfaces on  
508        both sides of the cataclasite - micro-structure - Breccias... - thick sections of  
509        the Breccias occur lenses which range from cm's to meters in thickness. Breccia  
510        clasts are typically poorly sorted and can be very coarse with clast up to 10 cm  
511        in diameter. Clasts show indications for multiple generations of brecciation.

512        Thin Quarts lens - iron wash

513        Systematic associations between fault rock and fault structure exist. For in-  
514        stance, Davatzes et al., 2002 reports of a systematic association between the fault  
515        rock lithology and the orientation of the fault set. Namely, the orthorhombic fault  
516        set striking WNW has systematic association with fragmentation—fault breccias;  
517        conversely the ENE fault set rather has slip surfaces cutting through deformation  
518        band clusters (see figure ??). This relation was speculated to be the result of  
519        contrasting genetic mechanism. The WNW set is the result of the reactivation of

520 regional joints. In contrast the ENE fault set is the the result of clustering and  
521 anastamosing deformation bands acting as a catalysing agent to the formation of a  
522 faults. In this study, we observe clear instance of lithological contacts being asso-  
523 ciated to brecciation (photo at iron wash where the top of the Navajo is brecciated  
524 and quickly reverts to a single fault strand. More over, large breccia bodies are  
525 clearly related to points where faults are cross-cutting each other at high obliquity  
526 as is often the case at the Chimney Rock fault array and

527 Complicating factors:

528 Associations between brecciation and lithological contacts...

529 Associations between brecciation and cross cutting faults...

530 For an extensive review and description of the faults in the Navajo and Entrada  
531 sand stones refer to Aydin's thesis.

### 532 **3.1 Interpretation of field observations and roughness mea- 533 surements**

534 Cross-cutting relationships reported bot in this study and in previous work on  
535 faults in the Navajo and Entrada units of the San-Rafael swell are particularly  
536 informative. Large displacement slip surfaces are not cross cut by deformation  
537 bands and more sinuous slip surfaces. However, large displacement slip surfaces  
538 do cross-cut clusters of deformation bands and more sinuous slip surfaces. This re-  
539 lationship is indicative of a clear evolution of the fault architecture by 1) localizing  
540 displacement and 2) smoothing out slip surfaces.

541 Faults zones with larger offset are associated to larger damage zones and more  
542 slip surfaces. This is particularly telling fact when with the observation that small

543 displacement slip surface do not cross cut larger displacement slip surfaces.

544 The cross cutting relationship implies that either slip either smaller less con-  
545 tinuous slip surfaces predate the onset of the larger offset slip surface or that the  
546 they splay off of it. However, we can reject the former as a possible mechanism as  
547 it does not account for the increased density of slip surfaces on larger offset fault  
548 zones. This implies that they either form directly from the stress heterogeneities  
549 induced by the roughness of larger displacement slip surfaces.

550 Slip surfaces pre-dating large The former case stress heterogeneities from active  
551 slip surfaces induced by fault roughness.

552 faults are smoother than joints or deformation bands

553 At the grains scale, grains are truncated, not ‘plucked’.

554 more linear fault traces where not offset by wavier fault traces

## 555 4 Geometric analysis

### 556 4.1 Method

557 This study focuses on the qualitative and quantitative evolution of fault slip sur-  
558 faces—both addressing how fault slip surfaces evolve and the implications thereof.

559 The quality of the displacement measurements and the large number of accurate  
560 surface scans are fundamental to the quantitative analysis of the data. Field-  
561 method and data acquisitions thus reflect these standards.

562 For the qualitative analysis, we carefully record the characteristics of the fault  
563 architecture in the context of fault evolution. Specifically, we are particularly  
564 meticulous about 1) identifying cross-cutting relationships which indicate temporal

565 evolution on the on fault, 2) identifying the evolutionary stages in the formation  
566 of faults and 3) identifying and characterizing the wear product, or fault rock,  
567 produce as faults evolve.

568 For the quantitative analysis, we collect scans both *in situ* and from hand  
569 samples collected in the field. Scans are associated to a constraint on displacement.  
570 Moreover, for every scan, the time of day, location, quality, strike and dip of the  
571 fault slip surface as well as the rake of the slickenlines are recorded. When possible  
572 we record an estimate of the fault rock thickness. Finally, we also record both a  
573 plan and cross-sectional view image of the scanned fault surfaces. See appendix  
574 for the tabulation of this data. Together, all these measurements and observations  
575 should provide the necessary data to robustly explain and quantify the process  
576 through which faults mature.

#### 577 4.1.1 Scan Data Acquisition

578 To measure slip surface roughness, we analyses large point clouds scans of real  
579 fault surfaces and average the slip parallel and perpendicular spectral and statis-  
580 tical properties across hundreds of profiles. Point clouds must be obtained across  
581 a flexible array of instruments to properly capture the fractal scaling behavior  
582 (Brown and Scholtz, 1985; Candela et al., 2012). In this study, we use three in-  
583 struments with complimentary scales of observation. Together, these instruments  
584 offer accurate and precise three-dimensional discretization of fault surfaces at over  
585 nine decades of length scale.

586 \*make a map of each areas with the location of every scan encoded with dif-  
587 ferent symbols\*

588 At the largest scales ranging from meters down to millimetres, a light detection

589 and ranging instrument (i.e. LiDAR). We use the LiDAR has been used in many  
590 previous studies of fault roughness as it is easily deployable in the field and provides  
591 rapid means to collet very large point cloud data set. However, its use is limiting  
592 as it requires exceptionally good and, accordingly, rare exposure of fault surfaces  
593 that are large enough and fresh enough to not have been degraded by erosion. In  
594 this study, we report 5 ??? Lidar Scans (see figure).

595 Instead, the bulk of in situ field measurements were made at intermediate scales  
596 ranging from centimeters down to hundreds of microns with the NextEngine 3D  
597 laser scanner. The NextEngine laser scanner is accurate down to 100 microns with  
598 resolution up to 41 540 points per square centimeter. Note that the NextEngine  
599 is a much less cost prohibitive option when compared to the LiDAR yet captures  
600 the same characters of the fault surfaces. The laser scanner was benchmarked to  
601 a machined-flat granite surface and to a scan of the corona slip surface both to  
602 industrial-grade laser scanner as reference. The scanner is not exactly built to be  
603 field ready. It requires a power source, low light conditions, a stable surface to  
604 sit on, limited dust exposure and must be connected to a computer. Moreover  
605 it only allows for a very limited depth of field. To use the scanner in the field,  
606 we connected both the laser scanner and laptop to a solar powered, *goal zero*,  
607 battery. The scanner was encased and padded in a reinforced cardboard box with  
608 its depth exactly equivalent to the optimal depth of field. The set up had the added  
609 advantage of being very portable, completely removing sunlight and limiting dust  
610 exposure. We report XXX scans using the NextEngine Laser scanner.

611 Finally, hand samples were collected and analyzed with the Zygo blah blah,  
612 an optical profilometer enabling accuracy from milimeters down to sub-micron.  
613 The Zygo blah blah uses white light interferometry to produce relatively small

614 point-clouds (XXX points) at various magnifications. It does however allow for  
615 seamless stitching of scans. Individual and stitched scans using the profilometer  
616 were benchmarked to a silicon carbide reference machined flat to XXX meters.  
617 All samples were scanned at 20x magnification and stitched together to produce  
618 sections roughly XXX by XXX millimeters. In addition, samples were scanned  
619 at the lowest magnification to properly bridge the gap up to the laser scanner  
620 resolution. We report scans of XXX samples with the white light profilometer,  
621 XXX of which were taken from surfaces scanned in the field with the laser scanner.

#### 622 4.1.2 Constraining displacement

623 We associate every scan with a displacement constraint. At The Chimney Rock  
624 Fault Array and Big Hole Fault entire displacement profiles have been measured  
625 during previous mapping campaigns (i.e. Maarten shipton). At Iron wash, Horse  
626 Creek and Molly's Castle, Atilla Aydin's mapping identified clear offset markers  
627 where available. Base maps for all field locations were georeferenced using satellite  
628 images when necessary and used as a reference in the field to streamline scan data  
629 acquisition. Displacement was estimated after the field campaign using GPS  
630 locations collected in the field. Additional measurements using basic tape measure  
631 and compass triangulation methods were also obtained in the field.

632 Base maps only report stratigraphic throw or, in some cases, offset across *entire*  
633 fault zones. However, many slip surfaces, complex networks of deformation bands  
634 and sheared joints which partition offset across fault zone (see figure). We  
635 therefore make a distinction between *offset* across an entire fault and *displacement*  
636 across a single slip surface. Without good marker horizons and cross-sectional  
637 exposure, stratigraphic offset is accommodated across slip surfaces is ambiguous.

638 Offset across the entire fault zone therefore only serves as an upper-bound con-  
639 straint on displacement across a single slip surface slip surface. In XXX of XXX  
640 fault slip surface measurements, this is the best available constraint on displace-  
641 ment.

642 PUT THIS UNDER FIGURE "At Big Hole fault, two large-scale continuous  
643 strands of the fault, both accommodating meters of displacement exemplify this  
644 mechanism at a larger scale. In accordance, Shipton and Cowie, 2003 report large  
645 uncertainty on the partitioning of stratigraphic offset across the two strands".

646 We were able to reconstruct exact displacement in the following specific cases:  
647 1) If full cross sectional exposure indicates a single slip surface; 2) If cross-sectional  
648 exposure is good enough to clearly indicate an offset marker (lamella, cross-bedding  
649 or lithological contact) and its attitude, traceable to the slip surface exposure;  
650 or 3) if it is unambiguous that one principle slip surface is accommodating an  
651 overwhelming majority of fault offset, i.e. it is continuous, it has a layer of fault  
652 rock and unmistakably more linear and sharp than any other slip surface in the  
653 fault zone.

654 Errors on displacement estimates are either reported directly for previous work  
655 (i.e. 1m precision for Maerten's throw measurements and 5m for Shipton's off-  
656 set estimates) or conservative 10% error on displacement estimates measurements  
657 made directly in the field.

658 \*make a table regarding the different types of displacement constraints\*

659 known unknown equation assumptions N

660 - throw - assuming 60 deg dip, dip slip - throw, dip – assuming dip slip -  
661 throw, dip, rake – assuming constant displacement orientation - direct off-set –  
662 with different permutations . . .

663    **4.1.3 Scan data Processing**

664    I use point cloud spatial statistics to characterize and quantify active surface pro-  
665    cesses on faults. I developed a *MatLab* work flow to entirely automate data pro-  
666    cessing from the raw *.xyz* input format to the final statistical analysis:

667    1. Preprocessing

668        (a) manual inspection for coarsest defects

669        (b) Import *.xyz* data into *Matlab*

670        (c) Very coarse Height field filter

671        (d) Flatten points

672        (e) Grid data

673        (f) Orient grid along slip direction (using power spectral analysis

674        (g) Remove defects

675              i. Remove outliers in the height field

676              ii. Fractal model filter

677              iii. Remove abnormally flat (interpolated) sections

678    2. Processing

679        (a) Statistical analysis

680              i. Scale dependent *RMS*

681              ii. Scale dependent skewness

682              iii. Scale dependent kurtosis

683              iv. Scale dependent asymmetry

684 (b) Spectral Analysis

685 i. Fast Fourier Transform (FFT)

686 ii. Lomb-Scargle Periodogram

687 *make into figure, include bypasses and other recent additions*

688 Note that the general pre-processing workflow was slightly adapted according  
689 to the different instruments that where used in the study. These adaptation were  
690 mostly attributable to the quality of the data at the various scales of acquisition  
691 and the actual instrument specifications. Scans collected with the LiDAR required  
692 more extensive manual point removal to avoid features such as vegetation, spurious  
693 outlier and large defects to affect the quality of the preprocessing. Scans collected  
694 at the intermediate scale with the laser scanner easily followed this workflow.  
695 Finally, scan collected with the white light interferometer did required minimal  
696 preprocessing and where aligned manually at the time of data collection.

697 Before conducting a statistical analysis scan data must be pre-processed into a  
698 workable format. Scan data is a point cloud - a series of points with coordinates  
699  $x$ ,  $y$  and  $z$ . Scans reported in this study typically have  $10^6$  to  $10^7$  points. In raw  
700 form, the point clouds are randomly oriented, noisy and still contain instrumental  
701 and physical artefacts. Physical artefacts include cracks, eroded sections, and  
702 vegetation; instrumental artefacts include noise, smoothing and scattering. All  
703 these features must be removed. The process of manual removal is labour intensive  
704 and unfeasible for a data set of the scope presented in this study. I rather opt to  
705 automate this process. Only very large defects (defects that may substantially  
706 effect the quality of finding a true mean plane) are manually removed.

707 The surface must first both be flattened and aligned along slip. Linear trends

708 in the data induce an unwanted high frequency signal in data and also affect the  
 709 quality of later interpolation onto a grid. Thus,  $x$ ,  $y$ ,  $z$  data is rotated using  
 710 around the axis  $\mathbf{u}$  as determined by the normalized cross product between the  
 711 surface normal  $\mathbf{n}$  and a vector normal to a flat surface ( $\mathbf{n}_2 = [001]$ ):

$$\mathbf{u} = \mathbf{n} \times \mathbf{n}_2 / |\mathbf{n} \times \mathbf{n}_2|$$

712 with the rotation,

$$R = \cos \theta \mathbf{I} + \sin \theta [\mathbf{u}]_x + (1 - \cos \theta) \mathbf{u} \otimes \mathbf{u},$$

713 were  $[\mathbf{u}]_x$  is the cross product matrix of  $u$  and  $\otimes$  is the tensor product and  $I$  is  
 714 the identity matrix.

715 Fault surfaces are anisotropic. The direction of slip is preserved in the anisotropy  
 716 whereby the 'smoothest' direction is slip parallel and the 'roughnest' direction is  
 717 perpendicular to slip. The fault scan is rotated around the  $z$  axis such that the  
 718 direction of slip is along the  $x$  axis. The direction of slip is by decimating raw data  
 719 before iteratd steps of regridding, one-degree rotation and spectral analysis. In  
 720 the radial search, roughness is quanified as the integral of the log-weighted power  
 721 spectrum over the entire bandwidth of the sample surface. The angle associated  
 722 to the minimum in roughness is then identified as the direction of slip and sub-  
 723 sequently used to rotated the original flattened point cloud. The data is then  
 724 interpolated onto a grid using a linear interpolation algorithm. The point spacing  
 725 is automatically defined by the point density over the areal extent of the data:

$$\Delta x = N_{pts} / AXXXXXX \quad (6)$$

726        INCLUDE HISTOGRAMS FOR EACH FILTER

727        *Defects* include all physical surface features that are clearly not associated  
728        any faulting process, *e.g.* cracks, eroded patches, vegetation, etc.. Defects are  
729        identified and filtered out using combination of thresholding methods. These  
730        methods all revolve around identifying clear points or segments that are statistical  
731        outliers to the distribution characterizing the entire surface—abnormal points.

732        The most aggressive filter implemented searches for outliers to the fractal  
733        model. The filter removes entire linear segments with abnormally high variance  
734        in the height field for the given scale of observation. For this implementation, I  
735        iterate over 10 filter scales. The scales are selected using a log spacing from the 10  
736        points up to the length of the entire surface. The threshold for segment removal  
737        is chosen to be four standard deviations from the mean (should account for  $< 0.1$   
738        percent of the data in a normal distribution). Note that, assuming a normal distri-  
739        bution of variance data for a given scale, the filter should not induce a systematic  
740        bias since the filtering is symmetric around the mean. However, surface features  
741        associated with a truly distinct mechanism of formation, in this case cracks and  
742        other defects that will typically have much higher variance, *are* be removed. This  
743        general approach ensures that defects, regardless of their scale get identified and  
744        removed. This is important for any subsequent fractal analysis.

745        Abnormally flat sections arise as the result of triangular interpolation of sparse  
746        points. Typically, interpolation on the edge on a non-convex set of points is subject  
747        to this effect. These artefacts are readily identified in the curvature data. In the  
748        log-transformed absolute value curvature field, these sections appear to be nearly  
749        or exactly zero. The filter rejects point with curvatures less than  $10^{-25}$ . These  
750        values likely associated to the linear interpolation scheme.

751 Finally, all scan are inspected to make sure that the pre-processing was suc-  
752 cessful. The script fails to properly process scans that are excessively populated  
753 with surface defects. These scans were manually cleaned and oriented before re-  
754 processing them. Manual changes were executed in *CloudCompare*.

755 Pre-processed scans are  $N$  by  $M$  scalar fields of fault surface topography(the  
756 sitance from the mean plane) aligned with slip along the  $x$  axis. NaN values mark  
757 locations where data is missing or was removed by filters. Point spacing is defined  
758 the mean point density of the scan in the  $x$ - $y$  plane.

759 **4.1.4 Statistical Analysis**

760 After pre-processing, scans discretize defect-free slip surfaces with grids with rows  
761 aligned with the slip direction. We compute the power spectral density content for  
762 every continuous segment of every single profile of the grid using a Fast Fourier  
763 Transform (FFT). Individual spectra are interpolated onto a master frequency  
764 vector. For a given frequency, the distribution of power values across the pro-  
765 files through along the slip is strongly skewed (see figure xxx). The skewness is  
766 attributable to the non-negative constraint on power and residual outlying pro-  
767 files (defects not properly removed). To provide a more representative and robust  
768 measure of maximum likelihood, we use the geometrical mean instead of the arith-  
769 metical mean. Accordingly, errors represent the  $1\sigma$  range in the log-transformed  
770 distribution. The analysis yields one representative spectrum for each scan.

771 The spatial frequency content of slip surfaces follow a power law. This charac-  
772 teristic is roughly fixed for a single slip surface regardless of the scale sampled in  
773 our instrumental array. Fixed scaling and its power law form in frequency space is  
774 a feature of the fractal character of fault surfaces. We can thus further distil the

775 roughness measurements using the fractal model of the fault:

$$P(k) = Ck^{-\beta} \quad (7)$$

776 Accordingly the entire spectral information of a scan can be summarized with  
777 the prefactor ( $C$ ) and the scaling exponent ( $\beta$ ). Determining fractal parameters  
778 from spectra is not trivial. *A priori*, the fractal model is determined using a  
779 weighted power law regression through the spectra. Weights are determined ac-  
780 cording to the inverse  $1\sigma^2$  variance of the power estimates. However, confidence  
781 interval on the fit parameters are strongly sensitive to both instrumental and an-  
782 alytical biases (XXX schittbulh 1998). Biases induce unwanted high or low pass  
783 filters in the spectral content-amplifying or diminishing selective bandwidth. The  
784 combination of instruments and highly overlapping bandwidths provides a means  
785 to identify the affected sections and suppress methodological bias. The comparison  
786 of the power law fit through multiple heavily overlapping instrumental bandwidths  
787 to the representative spectral of individual scans highlights instrument-specific bi-  
788 ases. In doing so, we identify conservative bounds on sections of frequency spec-  
789 trum that deviated from the power law fit. For our instruments, we find that  
790 artefacts are particularly disruptive at the small scale instrumental limit. The  
791 LiDar and laser scanner are dominated by a shallower slope at the high frequency  
792 tail of the spectra which has been interpreted in previous studies as random noise  
793 (XXX). Conversely, the spectra of the scan collected using the white light interfer-  
794 meter have steeper high frequency tails. This artefact has not been reported in  
795 previous studies in spite of the extensive use of the instrument. This discrepancy  
796 is likely attributable to the comparatively limited and subdued use of aggressive

smoothing filters both in the scan data and in the spectra our analysis. Affected bandwidths are omitted from subsequent analysis. In spite of this approach, small discrepancies in parametrization of the power law fit for a given slip surface render the extrapolation of measurements from on instrumental bandwidth to the other instrumental scale of limited use. We therefore choose to report any further results at the bandwidth or specific wavelength best captured by the instrumental magnification.

INCLUDE A FIGURE WITH: ORIGINAL SURFACE, AUTOMATICALLY PROCESSED GRID, MANUALLY PROCESSED GRID AND CORRESPONDING POWER SPECTRA.

identifying fractal scaling section plot of white light all magnifications computational scheme to select the good section error on direct displacement estimates?

## 4.2 Results

### 4.2.1 Roughness measurements

figures to include:

- all spectra
- increasing anisotropy (two surfaces) - polar plot

Figure XXX shows the all the PSD calculations obtained from the scans collected in this study. Consistent with previous work, we find that the PSD spectra over the entire bandwidth reported in this study generally follow a power law scaling (a linear relation in log-log space). This feature corresponds to the constant fractal scaling. The scaling exponent and pre-factors are calculated using linear

819 least-squares fit of the spectra in log-log space. The Hurst exponent can then be  
820 obtained according to equation XXX.

821 In the slip perpendicular direction, Hurst exponents range from XXX to XXX,  
822 with an average value of 0.8ish; Prefactors range from XXX to XXX with an  
823 average value of XXX. In the slip parallel direction, Hurst exponents range from  
824 XXX to XXX, with an average value of 0.8ish; Prefactors range from XXX to  
825 XXX with an average value of XXX. Implicit to the pre-processing grid alignment,  
826 for any single scan the slip parallel direction is systematically smoother than the  
827 slip perpendicular direction indicating a clear surface anisotropy. The entire data  
828 set does however indicate an overlapping range in slip parallel and perpendicular  
829 directions. We also note that lower pre-factors are generally associated to lower  
830 Hurst exponents.

831 An evolution with displacement is weakly expressed in the spectral analysis but  
832 is cluttered and obscured by highly variable errors on displacements and rough-  
833 ness measurements. In order to highlight the effect of displacement on the sur-  
834 face roughness, we separate our scan data into two distinct populations. 1) Scan  
835 data with direct displacement constraint and 2) scan data associated to maxi-  
836 mum displacement constrains. Brodsky et al., 2011, tested the validity of a power  
837 law relation between fault roughness are various specific scales and displacement.  
838 Building upon this approach, we use both data populations to test the validity  
839 and parametrization of the fit and the Implicit hypothesis that faults smooth as  
840 a function of displacement—the smoothing model. Scan data with direct displace-  
841 ment constraints serves as a direct test and a means to parametrize the smoothing  
842 model. For the model to be valid it must agree with further constraints imposed  
843 by data with only maximum displacement estimates.

844 A point defined by the maximum error bound on displacement and the rough-  
845 ness of the fault surface is in agreement with smoothing model if it is rougher  
846 than roughness prescribed by the model as parametrized by direct measurement.  
847 Conversely, if the point is rougher than the model prediction, it is not physically  
848 possible in the model construct. A null hypothesis would prescribe no bound on  
849 the roughness and would simply have the predicted roughness of a fault be defined  
850 by the probability distribution function of the entire roughness dataset.

851 \* probably will revisit this \*

852 Accordingly, we can roughly estimate the probability that our distribution of  
853 data relative to the smoothing model is a random element of chance according to:

$$P = \prod p(y_i > Y(x_i)) \quad (8)$$

854

---

855 Figures XXX to XXX shows the relation between roughness and displacement  
856 as interpolated a various scales of observation. Vertical error bars on the power  
857 spectral density are obtained from the confidence interval of the of the fractal  
858 model regression. Horizontal errorbars on displacement are defined on a case by  
859 case basis from field observations and previous work in on the fault arrays. We  
860 present both the fit through the our entire dataset (comprised of direct and up-  
861 per bound constraints on displacement) and through the the directly constrained  
862 displacement estimates. Fits are obtained using a least squares linear regression  
863 through the log-transformed data sets. In order to provide error bounds on the  
864 fit parameters, we use a full Monte Carlo simulation sampling direct displacement  
865 estimated as Gaussian distributions, upper bound displacement constrains as com-

866 pletely random distributions across the entire possible range of displacements and  
867 power spectral density estimates as log normal distributions. Errors represent on  
868 standard deviation estimated from 10000 simulations.

869 The weak trend across the entire dataset imply and expectation of smoother  
870 slip surfaces in fault zones which have accommodated larger displacement.

871 Conversely the stronger trend across the well constrained data implies that an  
872 individual slip surface smooths with displacement. The smoothing exponent varies  
873 according to the different scales of observation (XXX at the laser at the centimeter  
874 scale, XXX at the milimeter scale and XXX at the micron scale). While a power  
875 law fit to the best constrained measurements is has poor fit metrics, we find a  
876 nearly perfect agreement with roughness measurements only associated to upper  
877 bound constraints.

878 Two constraints on displacement – two data populations plot of all the spectra  
879 color coded with displacement smoothing plots: parallel - $\zeta$  all scales perpendicular  
880 - $\zeta$  all scales Hurst exponent - $\zeta$  all scales Fit for smoothing through direct data,  
881 discuss consistency with max disp data Other statistical metrics? Poly-gaussian  
882 features in the surface roughness Skewness of height field as a function of scale  
883 Null result worth reporting? Do a plot of the evolution of skewness at the grain  
884 scale?

885 qualitative illustration of maturity

### 886 **4.3 Hard facts**

887 The following is a list of ‘hard facts’ that can be established from the both the  
888 qualitative and quantitative data:

- 889        • faults are smoother than joints or deformation bands
- 890            – power spectrum shows that fault slip surfaces are systematically smoother
- 891                than joint and deformation band surfaces at all wave lengths reported
- 892                in this study ( $10^{-6}$  to  $10^5$  meters)
- 893        • At the grains scale, grains are truncated, not ‘plucked’.
- 894        • The roughness of a slip surface is sensitive to its displacement history. This
- 895                result is robust across multiple faults both nucleated from deformation bands
- 896                and joints and variations in fault rock and host rock lithology.
- 897        • The smoothing exponent is likely more than 1 at certain scales - quote from
- 898                Emily: “In all of these cases, the scatter of the data is large, but the basic
- 899                result holds: the absolute value of the exponent is much less than 1.”
- 900        • The smoothing rate is highest at small displacements and decreases with
- 901                displacement.
- 902        • Smoothing occurs at all scales of this study
- 903        • a slip surface from a large offset fault is more likely to be smoother
- 904        • for any given the displacement on a fault, the smoothest slip surface roughly
- 905                follows the same smoothing trend as that defined by direct displacement
- 906                measurements.
- 907        • The roughness varies spatially on a slip surface - the scatter in the data
- 908                exceeds the instrumental error

- 909       • the height distribution of points on a slip surface can be far from normally  
910           distributed.
- 911       • the Hurst exponent has a very large range in values (less than Zero to 0.9)
- 912       • more linear fault traces where not offset by wavier fault traces

913       **5 Model**

914       In this study, we utilize work minimization and boundary element numerical mod-  
915       elling to capture the growth of fault damage and the effect of rough asperities.  
916       The modelling component is motivated by the following questions: can geomet-  
917       rical asperities fail through shear? In so doing, how do they fail?—and what are  
918       its sensitivities to asperity geometry and strength? Does strength heterogeneity  
919       and mechanical wear by the truncation of asperities properly capture the evolu-  
920       tion of fault slip surfaces with displacement. These questions prompt the need for  
921       physically robust models that can be accomodating of complex fault or asperity  
922       geometries. The complexity of these geometries imply that off fault damage will  
923       grow in complex stress conditions— conditions that are currently poorly captured  
924       by simple analytical solutions (e.g. [?]). Moreover, complexities related to the  
925       discontinuous nature of fracture are more simply captured by boundary element  
926       modelling than existing finite element or finite difference models. This simplicity  
927       arises from need of fewer, less sparse, sets of equations to solve ([?]). Limita-  
928       tions of the boundary elements approach for fault modelling and off fault damage  
929       predictions is the difficulty of accumulating offset. Maximum allowable offset is  
930       roughly half the length of boundary elements. Along with this complications is the

931 implicit trade off between model resolution and displacement. Approaches can be  
932 taken to circumvent the challenge however its development and implementation  
933 are beyond the current scope of this study.

934 The model builds off of fric2D and growth by optimization of work (GROW)  
935 developped by Michele Cooke and Jessica McBeck. Fric2D solves for displacement  
936 and stress conditions on fault elements with prescribed constitutive behaviours  
937 given prescribed boundary element stress boundary conditions and material prop-  
938 erties in two dimensions. Constitutive behaviour of fault elements are defined by its  
939 static and dynamic friction, critical slip distance, and shear and normal stiffness.  
940 In turn the behaviour of the medium fault elements and boundary elelements is  
941 linear elastic defined by Poisson's ratio and Yougn's modulus. For its part, GROW  
942 predicts fracture propagation paths. It does so by minimizing the external work on  
943 a system. As a natural analogue, the external work is the tectonic work imposed  
944 on a fault and its fault blocks, together comprising the system. The model allows  
945 for the simultaneous growth of multiple fractures. The general algorithm uses the  
946 same boundary element method as fric2D to describe the fractures–linear dislo-  
947 cation elements that discretize the entire length of the fault. As a crack grows,  
948 dislocation elements are added radially to the tip of the crack so as to minimize the  
949 external work on the system normalized by the crack area ( $W_{ext}/\Delta A$ ). External  
950 work is further defined as:

$$W_{ext} = \oint (\tau u_s + \sigma_n u_n) dB \quad (9)$$

951 External work is readily calculated from the the output of fric2D. Accordingly  
952 it is possible to iteratively test a range of directions of growth, compared the

953 external work required, and choose the energetically preferred direction of crack  
954 growth. This process continues until stress at the tip of the cracks is not sufficient  
955 to overcome the fracture toughness. Therein lies the general algorithm of GROW.

956 In practice GROW utilizes almost the same inputs as fric2D. The user must  
957 specify what points are considered to be 'flaws'. Only the coordinates associated  
958 to the flaws are analysed and allowed to grow according to the GROW algorithm.  
959 The computational cost of multiple initiation points is large. Every added flaw  
960 grows the computational cost exponentially according to the angular range and  
961 resolution. We rather use fric2D to educate the choice of coordinated for the flaws  
962 on the fault.

963 Stress conditions are assessed along the fault elements. Normal ( $\sigma_{11}$ ), shear  
964 ( $\sigma_{12} = \sigma_{21}$ ) and tangential ( $\sigma_2$ ) stresses on the fault elements yield the two di-  
965 mensional stress tensor. Its Eigenvalues in turn allow for the determinations of  
966 principle stresses ( $\sigma_1$  and  $\sigma_3$ ). These in turn allow for calculation of the Mohr  
967 Coulomb stress and the assessment of elements prone to failure in shear according  
968 to host rocks angle of internal friction ( $\phi$ ) and cohesion ( $c$ ).

$$\tau_m = \sigma_m \sin(\phi) + c \cos(\phi) \quad (10)$$

969 where,

$$\tau_m = \frac{\sigma_1 - \sigma_3}{2} \quad (11)$$

970 and,

$$\sigma_m = \frac{\sigma_1 + \sigma_3}{2}. \quad (12)$$

971 We also assess element that may fail in tension. Elements with least principle  
972 stress in tension exceeding the cohesive strength of the medium are also identified  
973 as being prone to fail. In the likely case that entire fault segments (multiple fault  
974 elements) are in stress conditions exceeding the failure criterion of the rock, we  
975 choose local maxima of Coulomb stress and tensile stress along these segments as  
976 the failure points.

977 This additional functionality is implemented in Matlab and seamlessly links  
978 fric2d, failure assessments and GROW into one single workflow.

## 979 **5.1 Model Results**

# 980 **6 Discussion**

### 981 **6.0.1 Tying the model together with roughness measurements and 982 model**

983 wear rate (character), tying together model with

### 984 **6.1 An external estimate of gouge production and fault 985 thickness \* this section will likely be removed**

986 The data collected in this study offers the unique opportunity to provide new  
987 indirect estimates of fault rock production, fault thickness and dilation rate over  
988 an entire fault. We know that 1) the primordial roughness is systematically rougher  
989 than mature faults, 2) the primordial roughness is relatively constant, and 3) the  
990 roughness can be estimated for a given displacement. Using these results, I will  
991 estimate the volume of fault rock produced through wear and the corresponding

992 roughness induced accomodation space in the fault system.

993 Displacing two rough fractal surface in shear requires dilation. The expectation  
994 dilation can be estimated according to the amplitude of the largest wavelength ( $\lambda$ )  
995 being offset (see figure XXX). For a given displacement,  $u$ , the largest wavelength  
996 in the system will be  $\lambda = 2u_i$ . Using a fractal paradigm to define the average  
997 amplitude of a given wavelength according to the pre-factor  $\beta$  and the Hurst  
998 scaling exponent,  $H$ , (\*reference the equation\*) we find that the dilation,  $A$  can  
999 be expressed as a function of displacement:

$$A(u) = \sqrt{\beta 2u^{-2H-1}} \quad (13)$$

1000 If we apply this to an entire fault system with displacement field,  $U$ , we can  
1001 estimate the void space that would be produced:

$$V_{void}(U) = \int_S \sqrt{\beta 2U^{-2H-1}} dS \quad (14)$$

1002 Since the fault system is closed any change in fault roughness *must* be coupled  
1003 to the fault core. If all changes in the fault surface are associated to a production  
1004 of fault rock, we can effectively estimate the volume of fault rock that has been  
1005 produced from diplacement  $u_0$  to  $u_f$  by comparing the volume integral under the  
1006 corresponding initial and final slip surfaces  $S(u_0)$  and  $S(u_f)$ .

$$\frac{\Delta V_{faultrock}}{\Delta u} = \int_S S(u_0) - S(u_f) dS \quad (15)$$

1007 volume integral under the surfaces,  $S$ , can be estimated numerically according  
1008 to the frequency distribution prescribed by the RMS the entire fault system. Note

1009 that the RMS is estimated at the length scale of the entire fault; wear processes  
1010 are active at all length scales below this.

$$\int S dS \approx \quad (16)$$

1011 Now for the displacement field,  $U$ , we can estimate the total fault rock produced  
1012 by using the primordial surface roughness,  $S(0)$ , and the prediction of the surface  
1013 roughness extrapolated to the length of the fault (\* reference the the equation of  
1014 smoothing \*) such that:

$$V_{faultrock}(U) = \int_S S(0) - S(U) dS \quad (17)$$

1015 The comparison between the two quatities is telling. If the amount of fault  
1016 rock is

## 1017 7 conclusion

### 1018 7.1 future work

## 1019 8 Appendix

### 1020 8.1 Surface Processing scripts

1021 Or possibly a link to a git repository...

1022    **8.2 User manual for script**

1023    This manual should serve as both a basic guide to the logic and usage of the *surface*  
1024    *processing package*.

1025    The master function of the package is *surfaceprocessing*. This function effec-  
1026    tively deal with the inputs and direct computations towards the necessary func-  
1027    tions. Outputs of the function are a .mat workspace file for each input data file.  
1028    The workspace includes a structure (called *parameters*) with the raw surface anal-  
1029    ysis outputs, the point spacing, the decimation factor (if any), the file name and  
1030    the date of the analysis. The workspace also includes the grid form of the origi-  
1031    nal inputed surface (called *surface*), and the pre-processed copy that was used for  
1032    the subsequent analysis (called *zGrid*). Inputs are always included in pairs. The  
1033    former defines the type of input, the latter qualifies or quantifies the input. This  
1034    structure allows for adaptability of the code to various needs. Options include the  
1035    following:

1036    • *what to do?*: 'toDo', followed by the desired analyses on of: 'FFT', 'PLOMB',  
1037    'parameters' or 'all' (default is 'all') - can be a cell array. This specifies what  
1038    kind of spatial analysis will be done on the input surface data. The spatial  
1039    analysis is calculated and averaged across every single profiles along the  
1040    surface. The analyses are the following:

- 1041        – 'FFT', a power spectrum computed using a Fast Fourier Transform  
1042              (FFT) algorithm;
- 1043        – 'PLOMB', a power spectrum computed using a least-squares Lomb-  
1044              Scargle algorithm;

- 1045            – 'paramters', the calculation (as a function of scale) of the Root Mean  
 1046            Squared (RMS), skewness, kurtosis and asymmetry averaged across all  
 1047            segments of a given length on all profiles of the surface.
- 1048            'all' simply performs all the analyses outlined above.
- 1049     • *skip pre-processing?*: 'bypass', followed by 'zygo', 'pre-processing' or 'no' to  
 1050            be used input is already in aligned clean grid form - input files are then  
 1051            (default is 'no'). 'zygo' is specifically adapted to the proprietary data format  
 1052            of the white light in Wong. 'pre-processing' simply skips any pre-processing.  
 1053            This option requires a .mat structure with a field named 'grid' with the  
 1054            topography and a field name 'pointSpacing' specifying the point spacing (in  
 1055            meters). In either case the topography must be aligned such that the positive  
 1056            x direction is the parallel direction.
  - 1057     • *for the parameter analysis, how many scales?* 'numberOfScales' followed  
 1058            by the desired number of analysed scales. This option is relevant to the  
 1059            parameters analysis. Note that this has a lot of effect on the amount of  
 1060            processing time (default is 10).
  - 1061     • *decimation*: 'decimationFactor' followed by the desired decimation factor  
 1062            (default is 1). Decimation is a useful tool to reduce computation time. The  
 1063            surface grid is sub-sampled according to the decimation such that a decima-  
 1064            tion factor of  $k$  would imply that only every  $k$ th point on the every  $k$ th will  
 1065            be considered for hte subsequent analysis.
  - 1066     • *Instrument specific analysis* 'instrument' followed by 'white light', 'laser  
 1067            scanner' or 'lidar' (default does not set any instrument specific adjustments).

1068        Some instrument specific pre-processing steps are taken. Please contact me  
1069        if you intend to use this as they may be highly dependent on the specific  
1070        instrument used.

1071        For instance, *surfaceprocessing('todo','FFT','bypass','zygo')* will only perform  
1072        a power spectral density analysis and will skip preprocessing and assume that all  
1073        input will be in the 'zygo' export .xyz format.

1074        When the command is executed, the user will be prompted to navigate to the  
1075        directory where the input data is located. IMPORTANT: the directory must *only*  
1076        contain files of one data format. There cannot be other files or sub-directories  
1077        in the directory. The user will then be prompted to choose a destination for the  
1078        output data. The requirements for the output location are less stringent. However,  
1079        it is advisable to choose an empty directory such as to facilitate subsequent steps.

1080        The next step is to visualize the output of the analysis. This is done using the  
1081        *unpack parameters* function. This function provides various visualization options  
1082        for all files in the directory chosen by the user. The first input (the *desired plot*)  
1083        can be one of the following:

1084            'FFT': plot all power spectra;

1085            'PLOMB': periodogram plot as determined by the Lomb-Scargle least squares  
1086            analysis;

1087            'topostd': plot of the root mean squared (RMS) as a function of scale;

1088            'topoSkew': plot of skewness of height fields as a function of segment scale;

1089            'topoKurt': plot of the the kurtoisis of height fields as a function of segment  
1090            scale;

1091       'PowerVsDisp': plot of power interpolated at a given scale as a function of  
1092       displacement;

1093       'RMSVsDisp': model RMS at a given scale as a function of displacement

1094       'Grids': shows both the original and pre-processed grid for the specified file  
1095       'fileName';

1096       'Best Fits': best logarithmic fits to power spectra obtained from the fast  
1097       fourrier transform analysis.

1098       The functionality of the packages is broadly divided into three sections: 1)  
1099       importing and preprocessing data, 2) performing various spatial statistics on the  
1100       pre-processed data, and 3) unpacking the analysis output into figures.

1101       In order to run smoothly the all functions included in the package should be  
1102       kept in the same directory or on an accessible path.

1103       For reference, here is a quick outline of what each function does:

1104       `affine fit`: (from mathworks) Computes the plane of best fit using least  
1105       squares normal distance;

1106       `align grid`: finds the smoothest directions in a grid using FFT spectra and  
1107       rotates and re-grids the input grid;

1108       `fault spectral density simple`: Calculates the average lomb-scargle spectral  
1109       density every row of a N by M array;

1110       `FindErr loop anisotropy`

1111       `flatten XYZ`: removes planar trends from XYZ data by applying a rotations  
1112       matrix according to the best fit plane (`affine fit`);

1113        *fractal model outlier*: Removes outlying segments according to a near-gaussian  
1114        model for the distribution of RMS values at specified segment lengths (or  
1115        scales);

1116        *frequency spectrum*: Calculates the average lomb-scargle spectral density of  
1117        all continuous segments on every single row of a N by M array;

1118        *parse zygo format*: extracts the both the point spacing and topographic grid  
1119        from the exported zygo format. Can also remove planar trend from data  
1120        (substracted from grid);

1121        *rotateZ*: applies rotation matrix on XYZ data

1122        *surface analysis*: Aggregates the analysis functions and applies them to an  
1123        input grid

1124        *surface cleaning*: removes outliers associated to surface defects

1125        *surface parameters*: calculates spatial statistics and parameters along seg-  
1126        ments as a function of scale (RMS, skewness, directional asymmetry and  
1127        kurtosis)

1128        *surface preprocessing 2*: deals with preprocessing input data (import data,  
1129        cleaning and gridding data)

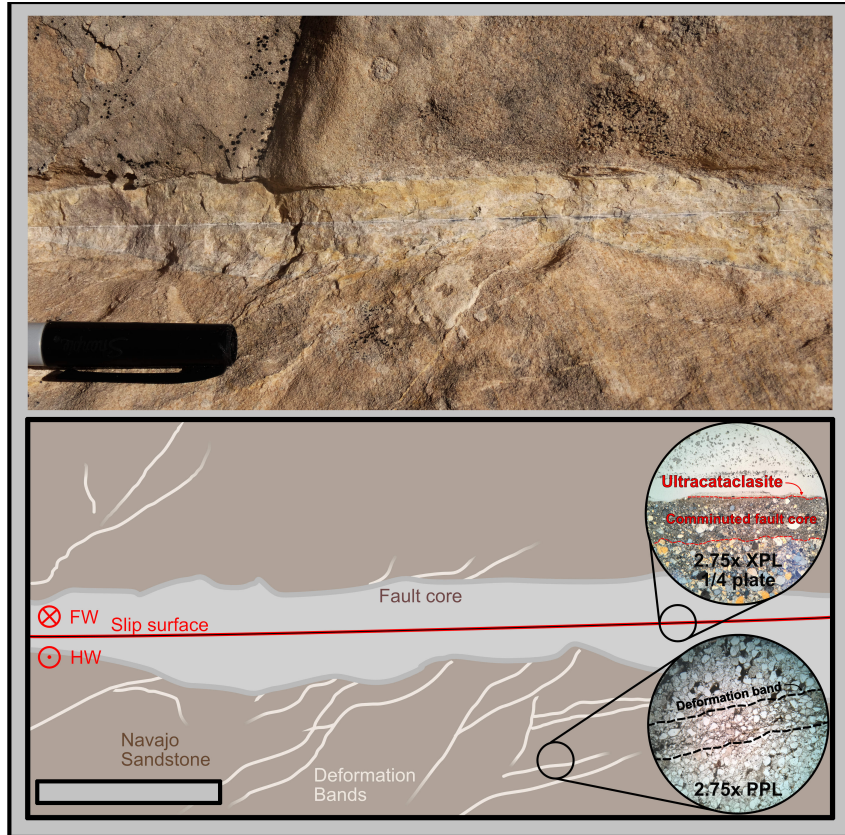


Figure 4: Top: Example of representative meso-structure of faults in the Navajo sandstone. Bottom: Cartoon of the representative meso-structure with slip surface (red), fault core (grey), deformation bands (pale beige) and intact host sand stone (brown). Upper half is the footwall; lower half is the hanging wall. Exposure is slip perpendicular. Representative thin sections show (not in situ) show the bottom half of the fault core (top) and deformation band (bottom). The section through the slip surface shows the microstructural architecture of slip surfaces with a very fine layer (barely visible) of ultra-cataclasite and a bounding comminuted layer. Note that this section is still well within the fault core. The section through the deformation bands shows the gradational reduction in grain size (outlined by black dashed line).



Figure 5: Left: Example of at least two distinct polished slip surfaces on the same fault structure. Right: Example of concentric pattern on cross-sectional view a fault

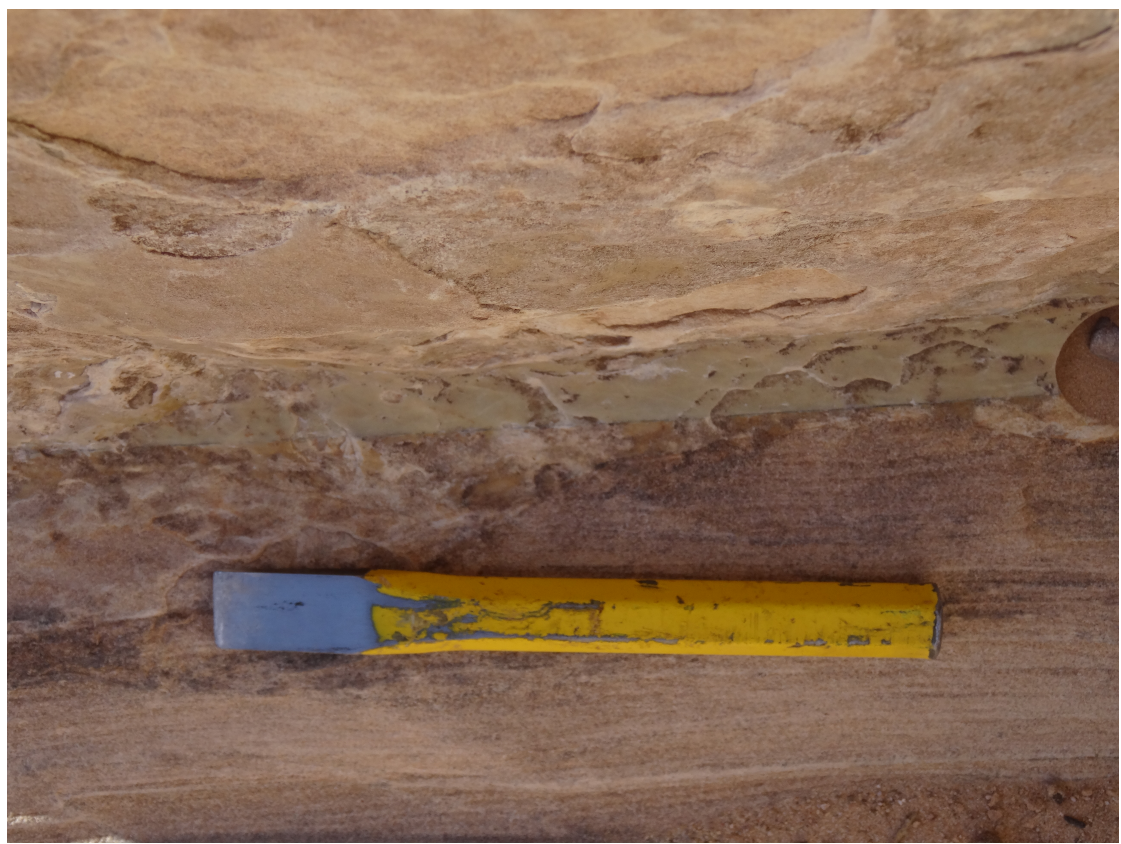


Figure 6: Example of a slip surface interpreted as a principle slip surface with around 20 meters of displacement at Big Hole Fault